Saturable absorption and visible pulse modulation of few-layer topological nodal-line semimetal HfGeTe

Qiming Zhao (赵启明)[1], Shouyan Zhang (张首焱)[1], Shuxian Wang (王树贤)[1*], Gang Wang (王 刚)[2**], Haohai Yu (于浩海)[1***], and Huaijin Zhang (张怀金)[1]

[1] State Key Laboratory of Crystal Materials and Institute of Crystal Materials, Shandong University, Jinan 250100, China

[2] Beijing National Laboratory for Condensed Matter Physics, Institute of Physics, Chinese Academy of Sciences, Beijing 100190, China

*Corresponding author: shuxianwang@sdu.edu.cn
**Corresponding author: gangwang@iphy.ac.cn
***Corresponding author: haohaiyu@sdu.edu.cn

Topological nodal-line semimetals attract growing research attention in the photonic and optoelectronic fields due to their unique topological energy-level bands and fascinating nonlinear optical responses. Here, to the best of our knowledge, we first report the saturable absorption property of topological nodal-line semimetal HfGeTe and the related pulse modulation in passively Q-switched visible lasers. Few-layer HfGeTe demonstrates outstanding saturable absorption properties in the visible-light band, yielding the saturation intensities of 7.88, 12.66, and 6.64 $\mu J/cm^2$ at 515, 640, and 720 nm, respectively. Based on an as-prepared few-layer HfGeTe optical switch and a Pr:LiYF$_4$ gain medium, Q-switched visible lasers are also successfully achieved at 522, 640, and 720 nm. The minimum pulse widths of the green, red, and deep-red pulsed lasers are 150, 125.5, and 420 ns, respectively. Especially for the green and red pulsed laser, the obtained pulse width is smaller than those of the low-dimensional layered materials. Our work sheds light on the application potential of topological nodal-line semimetals in the generation of visible pulsed lasers.

Keywords: visible pulsed laser; topological nodal-line semimetals; saturable absorption; Q-switching; Pr doping.
DOI: 10.3788/COL202422.031601

1. Introduction

Visible lasers are located in the visible-light band (380 nm to 760 nm) and manifest a wide range of important applications from scientific research to daily life, such as display, precision measurement, medical surgery, and optical communication[1–5]. In the past few decades, the generation of visible lasers has mainly been based on the nonlinear frequency conversion strategy from mature infrared lasers[6]. The invention of blue light-emitting diodes yielded the Nobel Prize in Physics in 2014 and made direct blue-laser-diode-pumped visible lasers possible[7]. Afterward, Pr-, Tb-, and Dy-based visible lasers aroused widespread research interest because they match good absorption of blue laser diodes and compact laser resonator design[8,9]. Along with the exploration of gain media, the continuous-wave blue-laser-diode-pumped visible lasers attain watt-level laser output[10]. In addition, pulsed visible lasers also attracted growing attention owing to their large energy density and high peak power, especially for the passive pulse modulation on the strength of saturable absorption[11–13]. Varieties of new-type visible saturable absorbers have been developed to enhance the relevant modulation properties[14]. Nonetheless, although different material optimization strategies have been implemented in thermal conductivity, saturation recovery time, broadband response, saturation power intensity, and pulsed modulation depth, the modulation performance of those saturable modulation devices remains unsatisfactory in the visible-light band so far[15].

Topological materials are one novel class of quantum materials with topological quantum states protected by space–time symmetry and have become a research hotspot in the fields of materials science and condensed matter physics[16]. More strikingly, topological materials exhibit fascinating physicochemical properties when space or time symmetry is broken, such as anomalous Hall effects, topological phase transitions, and topological superconductivity[17–19]. Topological insulators (Bi$_2$Se$_3$, Bi$_2$Te$_3$) and topological semimetals are also widely used as pulse laser modulators, but the modulation effect in the visible band is not satisfactory[20]. For example, graphene, as one representative of topological materials, has attracted widespread attention over the past decades due to its excellent optoelectronic properties[21]. Graphene owns zero bandgap, linearly dispersing Dirac points,

excellent thermal conductivity, high carrier mobility, and a short saturation recovery time[22–25]. Those enviable properties enable graphene to support broadband pulse modulation, which has been confirmed from the visible to the infrared regions. However, the absorption of monolayer graphene is only 2.3%, resulting in a low modulation depth[25,26]. The increase in layer number will bring additional unsaturated losses, which is not beneficial for the modulation performance of related pulsed lasers.

With the exploration of topological materials, topological nodal-line semimetals have been proposed in recent years[27]. The WHM-type (W = Hf, Zr; H = Ge, Si, Sn; M = Se, Te, O, S) topological nodal-line semimetals attracted great research interest due to their unique three-dimensional electronic band structure and novel physical phenomena, such as giant magnetoresistance, frequency-independent optical conductivity, and temperature-independent nodal-line plasmons[28–30]. Their Fermi velocities are comparable to graphene ($\sim 10^6$ m/s), and the related carrier recovery time (~ 0.6 ps) is much faster than that of graphene (~ 1.67 ps), indicating their sensitive response capability[25,31,32]. Moreover, the linear dispersion range near their Dirac points is approximately 2.5 eV, covering from the visible to the mid-/far-infrared bands[33]. Recent studies have verified the remarkable nonlinear response capability of WHM-type topological materials in nonlinear frequency conversion[34]. However, the saturable absorption and relevant pulse modulation of WHM-type nodal-line semimetals have not been studied so far. Here, we successfully prepared few-layer topological nodal-line semimetal HfGeTe and studied their saturable absorption properties in the visible-light region. On that basis, we performed relevant pulsed modulation at different visible wavelengths (522, 640, and 720 nm). The obtained results verified the application potential of the as-prepared few-layer nodal-line semimetal HfGeTe in the visible pulsed lasers, especially in the green-light band.

2. Experiments and Methods

The HfGeTe single crystals (Hf:Ge:Te = 1:0.92:1) were grown by a high-temperature solution method[35,36]. The obtained HfGeTe crystal was subjected to ultrasound in ethanol (30℃, 24 h) and centrifuged (6000 r/min, 5 min). The supernatant after centrifugation was directly spun onto quartz glass and silicon slice.

The morphology of the as-prepared HfGeTe samples was characterized by atomic force microscopy (AFM) (Dimension Icon, Bruker, Inc.). The Raman spectra of HfGeTe samples were characterized by a Raman spectrometer (iHR-550, Horiba, Inc.). The absorption spectra were investigated by a UV-visible-infrared spectrophotometer (UV-2600i, SHIMADZU, Inc.).

The nonlinear optical properties of HfGeTe/quartz glass samples were studied using the Z-scan technique. A 1030 nm femtosecond laser (200 fs, 100 kHz; BFL-1030-10H, Tianjin BWT, Inc.) equipped with a periodically polarized lithium niobate (PPLN) crystal was used as the pump source. The beam was
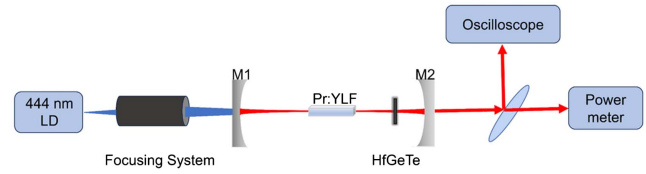

Fig. 1. *Q*-switched laser schematic design. Pr:YLF crystal, 444 nm; LD, LSR444SD, 3.5 W; M1, plane coating, $R_{444\text{ nm}} < 0.1\%$, concave coating, $T_{444\text{ nm}} > 99.9\%$, and $R_{522\text{ nm (640 nm or 720 nm)}} > 99.9\%$; M2, concave coating, $T_{522\text{ nm (640 nm or 720 nm)}} = 4\%$.

focused by a convex lens ($R = 50$ mm) and was irradiated onto the HfGeTe/quartz glass sample. The sample was placed on a computer-controlled linear mobile stage (M2DU-200 Stage, Data Ray, Inc.). The power transmitted through the sample was measured using a power meter (7N6153A sensor, Newport, Inc.).

As shown in Fig. 1, in the laser experiments a polished Pr:YLF laser crystal without coating (*a* cut, 0.43% doping concentration, 3 mm × 3 mm × 6 mm) was used as the gain medium. The input mirror (M1) and output coupling mirror (M2) were planar–concave mirrors with a radius of curvature of 50 mm. As shown in Fig. 1, the output average power was measured using the optical power meter (1919-R, MKS/Newport, Inc.). The pulse width and repetition rate of the pulsed laser were measured using an oscilloscope (TDS3012, Tektronix, Inc.).

3. Results and Discussion

3.1. Characterization of HfGeTe

As shown in Fig. 2(a), HfGeTe belongs to one kind of PbFCl-type (space group $P4/nmm$) structure, and the related crystal
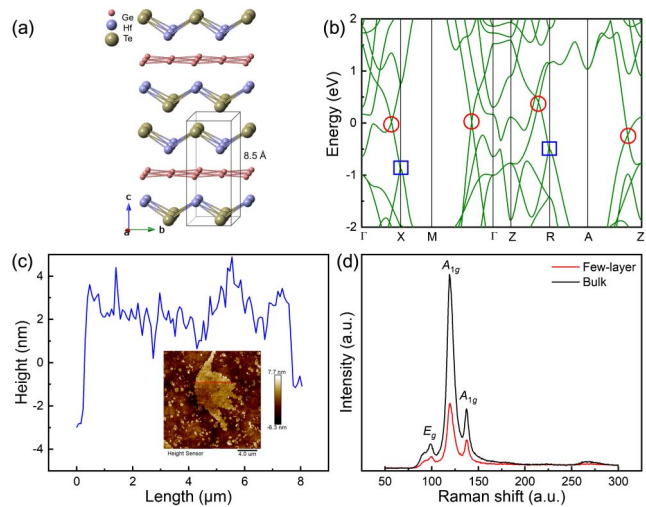

Fig. 2. (a) Crystal structure of HfGeTe; (b) bulk electronic structure of HfGeTe without spin-orbit coupling (SOC)[32,36,37]. Two kinds of Dirac points: red circle, a diamond-shaped Dirac nodal line; blue square, a quartic degenerated Dirac point. (c) Atomic force microscopy morphology of the HfGeTe/silicon slice; (d) Raman spectrum of the HfGeTe/silicon slice and HfGeTe bulk crystal.

growth is along the *c*-axis direction. The cleavage plane is an Hf-Te layer, and the single-layer cell thickness is about 8.5 Å. As shown in Fig. 2(b), the bulk electronic band structures of HfGeTe were calculated based on density functional theory[33,37,38]. It can be seen that the linear dispersion band region of the nodal-line Dirac points is relatively large (approximately 2.5 eV), which is conducive to the wideband absorption response covering from the visible regions to the mid-/far-infrared regions. As shown in Fig. 2(c), AFM was used to study the quality of the as-prepared few-layer HfGeTe sample. The surface was relatively uniform, and the related thickness was several nanometers. In addition, as shown in Fig. 2(d), two Raman spectrum modes existed in HfGeTe; one is ascribed to the motion in the *ab* plane [E_g mode (99 cm^{-1})], and the other is mainly due to the out-of-plane motion along the *c* axis [A_{1g} modes (119.5 and 137.3 cm^{-1})], which are consistent with the reported Raman vibrations of HfGeTe[33], indicating that the ultrasonic-treated sample still maintains the crystal structure of HfGeTe.

The saturable absorption mechanism at the Dirac points is described in Fig. 3(a). The electrons in the valence band are continuously excited into the conduction band, yielding a saturable absorption property. Finally, the Pauli exclusion principle blocks the interband transition, and the absorption reaches the saturation state. As shown in Fig. 3(b), the absorption spectrum of the as-prepared HfGeTe sample with quartz glass substrate was measured by comparing the absorption spectra of quartz glass. Compared with quartz glass, the as-prepared sample exhibits obvious absorption in the visible-light region. From that figure, it can be observed that the as-prepared HfGeTe/quartz glass sample has a wide-range response, from 300 to 1000 nm. This wide absorption range is attributed to the extremely narrow

bandgap of HfGeTe, which can be used as broadband saturable absorbers modulators for the visible-light band. To analyze the relationship between saturable absorption and wavelength, three different wavelengths (515, 640, 720 nm) were obtained by a 1030 nm femtosecond laser and a PPLN crystal. The saturable absorption properties of HfGeTe/quartz glass samples at those three different wavelengths were studied. The saturable absorption process was studied by a two-level analysis model, and the relationship of transmission versus power density can be described as[39]

$$T = A \exp\left(\frac{-\delta T}{1 + I/I_{\text{sat}}}\right),   \tag{1}$$

where T is the normalized transmittance of the experimental sample, I_{sat} is the saturation absorption intensity, δT is the absolute modulation depth of the experimental sample, I is the power intensity of the incident laser, and A is the constant of the experimental data. As shown in Fig. 3, the saturable absorption properties of the HfGeTe sample were measured at three different visible wavelengths (515, 640, 720 nm), and the experimental data were fitted using Eq. (1). The fitting results indicate that the modulation depth δT of the HfGeTe sample is 6.0% at 515 nm, 7.9% at 640 nm, and 5.9% at 720 nm. And the calculated saturation power intensity I_{sat} is 7.88 µJ/cm^2 at 515 nm, 12.66 µJ/cm^2 at 640 nm, and 6.64 µJ/cm^2 at 720 nm. The relatively larger absolute modulation depth and saturation intensity at 640 nm compared with the saturable absorption performance at 515 nm and 720 nm suggest that the HfGeTe sample might have better modulation potential at this wavelength.

3.2. *Q*-switched pulsed laser with saturable absorber HfGeTe

The output average power values of three different wavelengths versus pump power are shown in Fig. 4 (the inset is the lasing spectrum). The maximum *Q*-switched output power obtained is 28 mW (522 nm), 25 mW (640 nm), and 16 mW (720 nm), respectively. As shown in Fig. 4, for the three lasing wavelengths, their pulse repetition frequency shows a gradually increasing trend, while their pulse width shows a declining trend. The shortest pulse widths at three lasing wavelengths are obtained as the related output power reaches the maximum value, corresponding to the relevant largest repetition frequency. As shown in Fig. 5(a), the minimum pulse width of the 522-nm laser is 150 ns, which is smaller than those of $Co^{2+}:MgAl_2O_4$ (205 ns), $V^{3+}:YAG$ (440 ns), and MoS_2 (579 ns)[40-42]. As shown in Fig. 5(b), the smallest pulse width of the 640-nm laser is 125.5 ns, which is smaller than those of low-dimensional materials [MoS_2 (227 ns), Bi_2Se_3 (210 ns), monolayer graphene (709 ns), etc.][43-45]. As shown in Figs. 4(f) and 5(c), the minimum pulse width of the 720-nm laser is 420 ns, which is larger than that of Bi_2Se_3 (368 ns) and CdTe/Cds QDs (235 ns)[44,46]. In addition to the single-pulse waveforms of three different *Q*-switched lasers presented in Figs. 5(a)–5(c), the relatively uniform 640-nm pulse
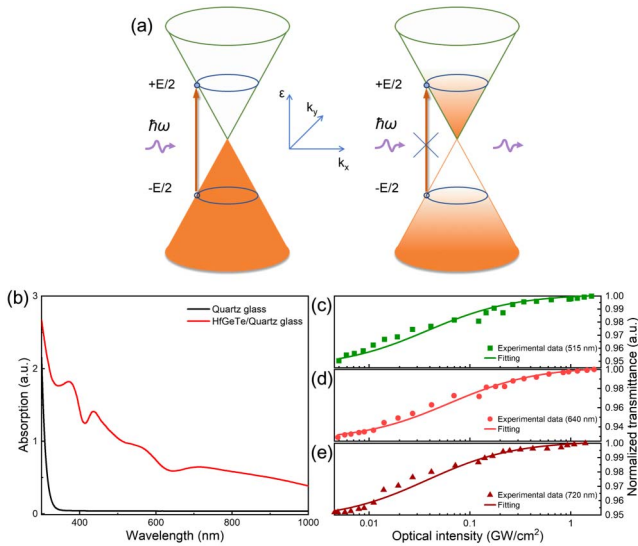

Fig. 3. (a) Schematic diagram of nonlinear saturable absorption at the Dirac point; (b) absorption spectra of the HfGeTe/quartz glass and quartz glass; relationship between transmittance and optical intensity at (c) 515 nm, (d) 640 nm, and (e) 720 nm, respectively.
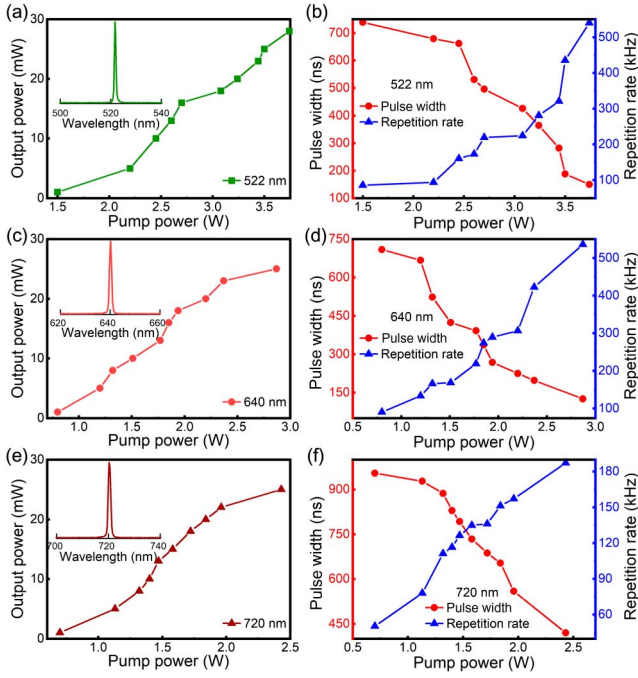
Fig. 4. Average output power versus pump power at (a) 522 nm, (c) 640 nm, and (e) 720 nm. The inserted figure is the related lasing spectra. Change of pulse width and pulse repetition frequency of the (b) 522-nm, (d) 640-nm, and (f) 720-nm Q-switched lasers.

train in Fig. 5(d) further indicates the excellent modulation performance of the HfGeTe saturable absorber.

As for Q-switched processes, the relationship of the pulse modulation depth δT and the pulse width τ_p could be represented by an analytical model of semiconductor saturable absorbers[47],
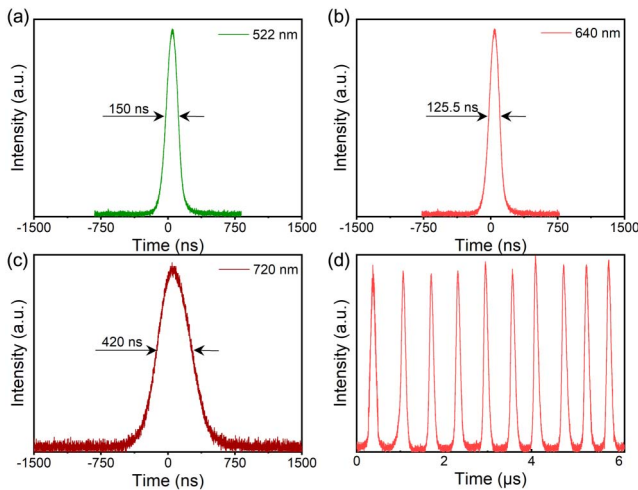

Fig. 5. (a) Pulse profile at 522 nm under a pump average power of 3.74 W; (b) pulse profile at 640 nm under a pump average power of 2.87 W; (c) pulse profile at 720 nm under a pump average power of 2.43 W; (d) pulse train of 640-nm pulsed laser under a pump average power of 2.87 W.

$$\tau_p = \frac{3.25 T_R}{\delta T}, \tag{2}$$

where T_R is the round-trip time. As measured in the above section, the saturable modulation depth of the HfGeTe sample was 6.0%, 7.9%, and 5.9% at the three different lasing wavelengths (522, 640, and 720 nm), respectively. In addition, the laser cavity of the three passively Q-switched lasers shows almost no change (145 mm). Based on the experimental data in Fig. 3(b) and Eq. (2), it can be concluded that the pulse modulation of the HfGeTe saturable absorber would demonstrate the smallest and largest pulse widths at 640 and 720 nm, respectively. The aforementioned laser results are consistent with the theoretical analysis. In addition, with the pulse repetition rate, pulse width, and output average power, the values of output pulse energy and output peak power can be calculated. As shown in Fig. 4, the maximum repetition frequency is 540 kHz (522 nm), 536 kHz (640 nm), and 187 kHz (720 nm), respectively. The maximum pulse energy is 51.9 nJ (522 nm), 46.6 nJ (640 nm), and 85.6 nJ (720 nm), respectively, which is comparable to the reported pulse energies of most two-dimensional materials. The output peak power corresponds to 0.35 W (522 nm), 0.37 W (640 nm), and 0.2 W (720 nm), respectively.

As Fig. 6(a) shows, the 640-nm saturation energy density of HfGeTe is 12.66 µJ/cm^2, which is comparable to those of semiconductor saturable absorber mirrors (SESAMs) but lower than those of some low-dimensional saturable absorbers. With respect to Pr^{3+}-based red pulsed lasers shown in Fig. 6(b), the as-prepared HfGeTe saturable absorber has a better modulation performance than those low-dimensional saturable absorbers in red-light bands even if under the close modulation depth (~10%). Moreover, few-layer nodal-line semimetal HfGeTe also yields a better modulation performance than those Co^{2+}- and V^{3+}-doped bulk crystals from the aspect of pulse width. Such a result verifies the application potential of this class of topological nodal-line semimetals in visible pulse modulation. We believe that the modulation performance of such
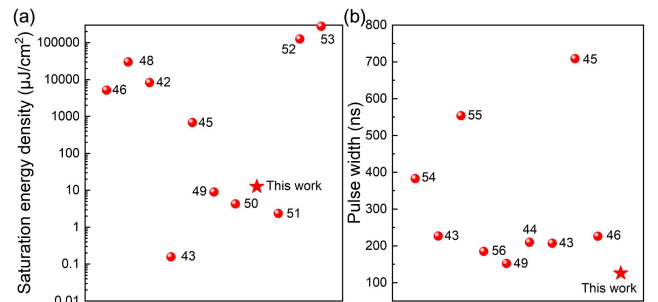

Fig. 6. (a) Saturation energy density of several low-dimensional saturable absorbers; (b) pulse widths of Pr-based red pulsed lasers based on different saturable absorbers; the numbers correspond to Refs. [42–46,48–56] (42, MoS$_2$; 43, WS$_2$; 44, Bi$_2$Se$_3$; 45, graphene; 46, CdTe/CdS quantum dots; 48, graphene oxide colloids; 49, Au nanorods; 50, few-layer MXene Ti$_3$C$_2$T$_x$; 51, 1T-titanium selenide; 52, Bi$_2$Se$_3$; 53, black phosphorus; 54, black phosphorus; 55, graphene oxide; 56, graphene).

kinds of saturable absorbers in the visible-light band can be further improved by optimizing material preparation and device design.

4. Conclusions

In summary, we prepared few-layer nodal-line semimetal HfGeTe and studied its saturable absorption properties in the visible-light band. Then, green (522 nm), red (640 nm), and deep-red (720 nm) pulsed visible lasers were successfully achieved using a few-layer HfGeTe saturable absorber. The as-prepared HfGeTe saturable absorber had a better modulation performance in green- and red-light bands. Especially for the green pulsed laser, the obtained minimum pulse width was 150 ns, which is superior to Co^{2+}- and V^{3+}-doped crystals and low-dimensional materials. To our knowledge, this is the first pulse modulation report of the topological nodal-line semimetal HfGeTe optical switch. Our obtained results indicate that the topological nodal-line semimetals have promising applications in the generation of visible pulsed lasers, which will broaden their application scope in the fields of photonics and optoelectronics.

Acknowledgements

References

1. B. C. Young, F. C. Cruz, W. M. Itano, *et al.*, "Visible lasers with subhertz linewidths," Phys. Rev. Lett. **82**, 3799 (1999).
2. C. E. Baker, "Laser display technology," IEEE Spectr. **5**, 39 (1968).
3. J. L. Hall, "Stabilized lasers and precision measurements," Science **202**, 147 (1978).
4. K. F. Gibson and W. G. Kernohant, "Lasers in medicine: a review," J. Med. Eng. Technol. **17**, 51 (1993).
5. C. T. Tsai, C. H. Cheng, H. C. Kuo, *et al.*, "Toward high-speed visible laser lighting based optical wireless communications," Prog. Quantum Electron. **67**, 100225 (2019).
6. M. M. Fejer, "Nonlinear optical frequency conversion," Phys. Today **47**, 25 (1994).
7. S. Nakamura, "Nobel lecture: background story of the invention of efficient blue InGaN light emitting diodes," Rev. Mod. Phys. **87**, 1139 (2015).
8. S. Luo, X. Yan, Q. Cui, *et al.*, "Power scaling of blue-diode-pumped Pr:YLF lasers at 523.0, 604.1, 606.9, 639.4, 697.8 and 720.9 nm," Opt. Commun. **380**, 357 (2016).
9. S. Ding, H. Ren, Y. Zou, *et al.*, "Single crystal growth and property investigation of Dy^{3+} and Tb^{3+} co-doped $Gd_3Sc_2Al_3O_{12}$ (GSAG): multiple applications for GaN blue LD pumped all-solid-state yellow lasers and UV or blue light chip excited solid-state lighting," J. Mater. Chem. C **9**, 9532 (2021).
10. M. He, S. Chen, Q. Na, *et al.*, "Watt-level Pr^{3+}:YLF deep red laser pumped by a fiber-coupled blue LD module or a single-emitter blue LD," Chin. Opt. Lett. **18**, 011405 (2020).
11. C. Körner, R. Mayerhofer, M. Hartmann, *et al.*, "Physical and material aspects in using visible laser pulses of nanosecond duration for ablation," Appl. Phys. A **63**, 123 (1996).
12. T. J. Allen and P. C. Beard, "High power visible light emitting diodes as pulsed excitation sources for biomedical photoacoustics," Biomed. Opt. Express **7**, 1260 (2016).
13. Z. Luo, D. Wu, B. Xu, *et al.*, "Two-dimensional material-based saturable absorbers: towards compact visible-wavelength all-fiber pulsed lasers," Nanoscale **8**, 1066 (2016).
14. J. Zou, Q. Ruan, X. Zhang, *et al.*, "Visible-wavelength pulsed lasers with low-dimensional saturable absorbers," Nanophotonics **9**, 2273 (2020).
15. H. Tanaka, S. Kalusniak, M. Badtke, *et al.*, "Visible solid-state lasers based on Pr^{3+} and Tb^{3+}," Prog. Quantum Electron. **84**, 100411 (2022).
16. B. Yan and S. C. Zhang, "Topological materials," Rep. Prog. Phys. **75**, 096501 (2012).
17. H. Weng, R. Yu, X. Hu, *et al.*, "Quantum anomalous Hall effect and related topological electronic states," Adv. Phys. **64**, 227 (2015).
18. C. Mondal, C. K. Barman, A. Alam, *et al.*, "Broken symmetry driven phase transitions from a topological semimetal to a gapped topological phase in SrAgAs," Phys. Rev. B **99**, 205112 (2019).
19. M. Sato and Y. Ando, "Topological superconductors: a review," Rep. Prog. Phys. **80**, 076501 (2017).
20. D. Wu, Z. Cai, Y. Zhong, *et al.*, "635-nm visible Pr^{3+}-doped ZBLAN fiber lasers Q-switched by topological insulators SAs," IEEE Photon. Technol. Lett. **27**, 2379 (2015).
21. K. S. Novoselov, A. K. Geim, S. V. Morozov, *et al.*, "Two-dimensional gas of massless Dirac fermions in graphene," Nature **438**, 197 (2005).
22. M. Sprinkle, D. Siegel, Y. Hu, *et al.*, "First direct observation of a nearly ideal graphene band structure," Phys. Rev. Lett. **103**, 226803 (2009).
23. P. Kumar, F. Shahzad, S. Yu, *et al.*, "Large-area reduced graphene oxide thin film with excellent thermal conductivity and electromagnetic interference shielding effectiveness," Carbon **94**, 494 (2015).
24. L. A. Ponomarenko, R. Yang, T. M. Mohiuddin, *et al.*, "Effect of a high-κ environment on charge carrier mobility in graphene," Phys. Rev. Lett. **102**, 206603 (2009).
25. Q. Bao, H. Zhang, Y. Wang, *et al.*, "Atomic-layer graphene as a saturable absorber for ultrafast pulsed lasers," Adv. Funct. Mater. **19**, 3077 (2009).
26. R. R. Nair, P. Blake, A. N. Grigorenko, *et al.*, "Fine structure constant defines visual transparency of graphene," Science **320**, 1308 (2008).
27. C. Fang, H. Weng, X. Dai, *et al.*, "Topological nodal line semimetals," Chin. Phys. B **25**, 117106 (2016).
28. R. Singha, A. K. Pariari, B. Satpati, *et al.*, "Large nonsaturating magnetoresistance and signature of nondegenerate Dirac nodes in ZrSiS," Proc. Natl. Acad. Sci. **114**, 2468 (2017).
29. M. B. Schilling, L. M. Schoop, B. V. Lotsch, *et al.*, "Flat optical conductivity in ZrSiS due to two-dimensional Dirac bands," Phys. Rev. Lett. **119**, 187401 (2017).
30. S. Xue, M. Wang, Y. Li, *et al.*, "Observation of nodal-line plasmons in ZrSiS," Phys. Rev. Lett. **127**, 186802 (2021).
31. Y. Liu, G. Dhakal, A. P. Sakhya, *et al.*, "Ultrafast relaxation of acoustic and optical phonons in a topological nodal-line semimetal ZrSiS," Commun. Phys. **5**, 203 (2022).
32. Z. Cheng, Z. Zhang, H. Sun, *et al.*, "Visualizing Dirac nodal-line band structure of topological semimetal ZrGeSe by ARPES," APL Mater. **7**, 051105 (2019).
33. Q. Zhao, L. Chen, F. Liang, *et al.*, "Angular engineering strategy for enhanced surface nonlinear frequency conversion in centrosymmetric topological semimetal $HfGe_{0.92}Te$," Adv. Mater., in press (2024).
34. S. Chi, F. Liang, H. Chen, *et al.*, "Surface nonlinear optics on centrosymmetric Dirac nodal-line semimetal ZrSiS," Adv. Mater. **32**, 1904498 (2020).
35. L. Chen, L. Zhou, Y. Zhou, *et al.*, "Multiple Dirac points including potential spin-orbit Dirac points in nonsymmorphic $HfGe_{0.92}Te$," Sci. China Phys. Mech. Astron. **66**, 217011 (2023).
36. P. C. Canfield, T. Kong, U. S. Kaluarachchi, *et al.*, "Use of frit-disc crucibles for routine and exploratory solution growth of single crystalline samples," Philos. Mag. **96**, 84 (2016).
37. W. Kohn, "Nobel Lecture: Electronic structure of matter-wave functions and density functionals," Rev. Mod. Phys. **71**, 1253 (1999).

38. G. Kresse and J. Furthmüller, "Efficient iterative schemes for *ab initio* total-energy calculations using a plane-wave basis set," Phys. Rev. B **54**, 11169 (1996).

39. W. D. Tan, C. Y. Su, R. J. Knize, *et al.*, "Mode locking of ceramic Nd:yttrium aluminum garnet with graphene as a saturable absorber," Appl. Phys. Lett. **96**, 031106 (2010).

40. M. Demesh, D. T. Marzahl, A. Yasukevich, *et al.*, "Passively Q-switched Pr:YLF laser with a Co^{2+}:$MgAl_2O_4$ saturable absorber," Opt. Lett. **42**, 4687 (2017).

41. L. Ollenburg, H. Tanaka, and C. Kränkel, "New saturable absorbers for Q-switched visible lasers," in *Laser Congress 2020 (ASSL, LAC)* (2020), paper ATu2A.6.

42. Y. Zhang, S. Wang, D. Wang, *et al.*, "Atomic-layer molybdenum sulfide passively modulated green laser pulses," IEEE Photon. Technol. Lett. **28**, 197 (2016).

43. Z. Luo, D. Wu, B. Xu, *et al.*, "Two-dimensional material-based saturable absorbers: towards compact visible-wavelength all-fiber pulsed lasers," Nanoscale **8**, 1066 (2016).

44. S. Luo, X. Yan, B. Xu, *et al.*, "Few-layer Bi_2Se_3-based passively Q-switched Pr: YLF visible lasers," Opt. Commun. **406**, 61 (2018).

45. Y. Zhang, Y. Yang, L. Zhang, *et al.*, "Watt-level continuous-wave and passively Q-switched red lasers pumped by a single blue laser diode," Chin. Opt. Lett. **17**, 071402 (2019).

46. B. Xu, S. Luo, X. Yan, *et al.*, "CdTe/CdS quantum dots: effective saturable absorber for visible lasers," IEEE J. Sel. Top. Quantum Electron. **23**, 1900507 (2016).

47. G. J. Spühler, R. Paschotta, R. Fluck, *et al.*, "Experimentally confirmed design guidelines for passively Q-switched microchip lasers using semiconductor saturable absorbers," J. Opt. Soc. Am. B **16**, 376 (1999).

48. N. Liaros, P. Aloukos, A. Kolokithas-Ntoukas, *et al.*, "Nonlinear optical properties and broadband optical power limiting action of graphene oxide colloids," J. Phys. Chem. C **117**, 6842 (2013).

49. S. Wang, Y. Zhang, J. Xing, *et al.*, "Nonlinear optical response of Au nanorods for broadband pulse modulation in bulk visible lasers," Appl. Phys. Lett. **107**, 161103 (2015).

50. Q. Yang, F. Zhang, N. Zhang, *et al.*, "Few-layer MXene $Ti_3C_2T_x$ (T= F, O, or OH) saturable absorber for visible bulk laser," Opt. Mater. Express **9**, 1795 (2019).

51. B. Yan, B. Zhang, H. Nie, *et al.*, "Broadband 1T-titanium selenide-based saturable absorbers for solid-state bulk lasers," Nanoscale **10**, 20171 (2018).

52. F. Gao, G. Zhang, Y. Liu, *et al.*, "Dual-loss-modulated Q-switched YVO_4/Nd:YVO_4 laser based on both Bi_2Se_3 and Cr^{4+}:YAG," Optik **265**, 169493 (2022).

53. D. Lu, Z. Pan, R. Zhang, *et al.*, "Passively Q-switched ytterbium-doped $ScBO_3$ laser with black phosphorus saturable absorber," Opt. Eng. **55**, 081312 (2016).

54. D. Wu, Z. Cai, Y. Zhong, *et al.*, "Compact passive Q-switching Pr^{3+}-doped ZBLAN fiber laser with black phosphorus-based saturable absorber," IEEE J. Sel. Top. Quantum Electron. **23**, 0900106 (2016).

55. Y. Zhong, Z. Cai, D. Wu, *et al.*, "Passively Q-switched red Pr^{3+}-doped fiber laser with graphene-oxide saturable absorber," IEEE Photon. Technol. Lett. **28**, 1755 (2016).

56. S. Kajikawa, M. Yoshida, O. Ishii, *et al.*, "Visible Q-switched pulse laser oscillation in Pr-doped double-clad structured waterproof fluoride glass fiber with graphene," Opt. Commun. **424**, 13 (2018).